How to cite: *Angew. Chem. Int. Ed.* **2025**, e202506448
doi.org/10.1002/anie.202506448

Polymer Brush

Nanoengineering Carbon Dot-Polymer Brush Interfaces for Adaptive Optical Materials

Gozde Aktas Eken, Nikolaos Chalmpes, Yuming Huang, Emmanuel P. Giannelis, and Christopher Ober**

Abstract: We present a versatile platform for fabricating two-photon excitable carbon dot-based nanocomposite thin films by harnessing the structural versatility of polymer brushes in combination with electron-beam lithography (EBL). This approach enables the precise spatial organization of carbon dots (CDs) at the nanoscale, facilitating dynamic modulation of their photoluminescent properties in response to environmental stimuli. Three model systems were examined, incorporating pH- and thermally responsive polymers, functionalized through covalent and dynamic covalent bonding strategies. By leveraging the spatial control afforded by nanostructured polymer brushes, we achieved precise tuning of optical properties while mitigating aggregation-induced quenching, a longstanding challenge in solid-state CD applications. In addition to the advances in controlling optical properties, this work highlights the potential of polymer brush systems to function as optically active, reprogrammable surfaces. The resulting nanoscale-engineered materials exhibit highly responsive, reconfigurable photonic behavior, offering a scalable pathway for integrating advanced optical interfaces into microchip technologies, biosensing platforms, and multiplexed diagnostic systems. The fusion of polymer brushes, carbon dots, and advanced lithographic techniques marks a substantial advancement in the development of functional materials with nanoscale precision and stimuli-responsive properties.

Introduction

Hybrid materials, incorporating nanoscale particles within a secondary phase or matrix, provide a versatile platform for engineering multifunctional systems.[1,2] By harnessing the dynamic interplay of optical, electrical, and mechanical properties, these materials offer enhanced functionality, adaptability, and performance across a wide spectrum of applications.[3,4] Nanofabrication techniques further enable the precise construction of hybrid micro- and nanoarrays, with meticulous control over features such as shape, size, and pitch distance.[5] These finely engineered structures deliver significant advantages in various domains.[6–8]

Carbon dots (CDs), a rapidly emerging class of carbon-based nanomaterials, have attracted significant attention due to their exceptional optical properties that rival those of semiconductor materials, including high quantum yields, remarkable resistance to photobleaching, and tunable photoluminescence (PL).[9] Their inherent biocompatibility, minimal environmental footprint, and cost-effective, scalable synthesis further enhance their appeal.[10] Typically classified as zero-dimensional (0D) nanoparticles with diameters below 10 nm, CDs feature a carbonized core surrounded by a functionalized surface or shell enriched with diverse functional groups or short polymer chains.[11] Recent advancements in synthetic strategies—particularly bottom-up approaches—have expanded the applications of carbon dots (CDs) by enabling precise control over their chemical composition and optical properties.[12–15] However, one of the major challenges hindering their practical applications is the quenching of photoluminescence at high concentrations or in solid-state forms. This phenomenon, referred to as aggregation-caused quenching (ACQ), results from fluorescence resonance energy transfer (FRET) and π–π stacking interactions between adjacent CD molecules, leading to a significant reduction in fluorescence intensity.[16] As a result, extensive research efforts have been devoted to mitigating ACQ effects, focusing on optimizing CD dispersion in solvents and developing innovative strategies to preserve their luminescent properties in concentrated systems or solid-state environments.[17,18]

For solid-state applications, CDs have been embedded in matrices such as polymers[19] inorganic salts,[20] and mesoporous or layered materials[21,22] to prevent aggregation. Leveraging CDs as fundamental building blocks, researchers have developed a diverse array of nanocomposite materials that exhibit a range of desirable properties, making them well-suited for applications in light-emitting diodes,[17] photovoltaic cells,[23] cell imaging,[24] cancer therapy,[25] sensors,[26] optoelectronic devices,[27] lasers,[28] and actuators.[29] Although embedding CDs into matrices enables their use in solid-state films, patterning methods that

[*] G. A. Eken, N. Chalmpes, E. P. Giannelis, C. Ober
Materials Science and Engineering, Cornell University, Ithaca, NY 14853, USA
E-mail: ga352@cornell.edu
cko3@cornell.edu

Y. Huang
Querrey Simpson Institute for Bioelectronics, Center for Bio-integrated Electronics, Northwestern University, Evanston, IL 602028, USA

Additional supporting information can be found online in the Supporting Information section

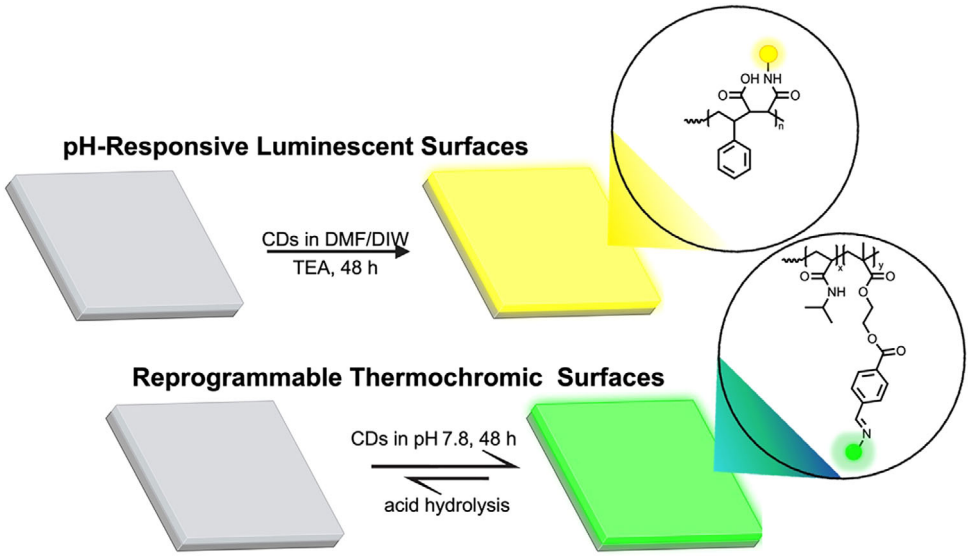

Scheme 1. Preparation of pH-Responsive and thermochromic surfaces via carbon dot immobilization on brush-modified substrates.

have been used so far—such as pen inks,[30] laser direct writing,[31] inkjet[32] and silk-screen printing,[33] fall short in precision, durability, and nanoscale resolution compared to lithographic techniques. Moreover, the integration of fabrication methods compatible with nanocomposites and other key materials remains largely unexplored, posing a significant challenge in establishing robust functional connections between device components.[34,35] Addressing this gap is a critical challenge, as it demands the development of fabrication techniques capable of achieving nanoscale precision while synergizing the responsive properties of matrices with the exceptional optical features of CDs.

Polymer brushes, featuring tunable and responsive architectures, offer versatile platforms for precise spatial control at interfaces, with their 3D structure enabling high-density nanomaterial immobilization that outperforms conventional monolayers. [36–38] Recent advances in nanofabrication and brush synthesis have enabled the precise patterning of polymer brushes with sub-50 nm features, a resolution critical for the accurate definition and spatial positioning of complex nanometric objects within functional systems.[39–42] By integrating nanomaterials with diverse chemical functionalities and leveraging the precise patterning capabilities and responsiveness of polymer brushes, it is possible to achieve synergistic and emergent properties that surpass those of the individual components.[43–47]

In this work, we present a versatile approach for fabricating carbon dot-based, stimuli-responsive nanocomposite thin films leveraging the unique capabilities of polymer brushes and electron-beam lithography (EBL). Polymer brushes with complementary functional groups were utilized to fabricate topographical templates, enabling the integration of stimuli-responsive components while ensuring precise regulation of the local concentration and spatial distribution of CDs (Scheme 1). Three model systems are explored, incorporating pH- and thermo-responsive structures capable of undergoing reversible optical changes in response to specific external stimuli. These systems are based on copolymers derived from specific monomer pairs: styrene-maleic anhydride (pSMA), 2-hydroxyethyl methacrylate (HEMA)-*N*-isopropylacrylamide (p(NIPAM-*co*-HEMA)), each engineered with distinct immobilization strategies—covalent and dynamic covalent bonds (Scheme S1). Luminescent films that are covalently anchored to substrate surfaces yield robust, dissolution-resistant thin films capable of withstanding postfabrication treatments while maintaining long-term stability and durability—key attributes for practical applications. Our approach enables the fabrication of intricate patterns that are composed of dissimilar materials with well-defined nanoscale features, collectively exhibiting dynamic functionalities in response to external stimuli. The precise regulation of optical response and reprogrammable chemistries presents significant opportunities for applications in microchip design, biosensing, and multiplexed diagnostics.

Results and Discussion

Synthesis and Characterization of Carbon Dots

Amine-functionalized CDs were synthesized via controlled pyrolysis of citric acid and ethylene diamine, following a previously established method.[48] Transmission electron microscopy (TEM) analysis (Figure 1a) confirmed the formation of well-dispersed spherical nanoparticles with an average diameter of 6–10 nm. X-ray photoelectron spectroscopy (XPS) analysis (Figure S1) was conducted to determine the chemical bonding states and surface functionalities of the CDs. The N 1 s spectrum provided clear evidence of nitrogen incorporation from the precursor, displaying two peaks at 400.1 and 402 eV, corresponding to NH_2 (93%) and NH_3^+ (7%), respectively.[48,49]

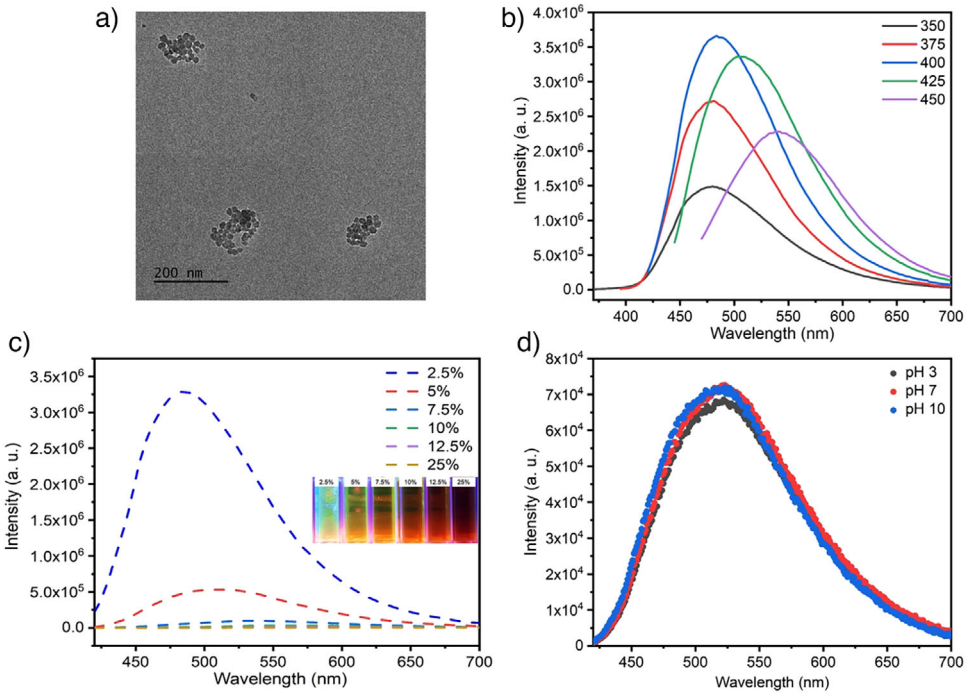

Figure 1. Morphology and optical properties of CDs. a) TEM image of CDs, b) The excitation-dependent PL spectra, and c) PL spectra of CD solutions with varying concentrations (wt%) d) PL spectra of CDs in buffer solutions with various pH values ($\lambda_{ex} = 400$ nm).

The excitation-dependent photoluminescence (PL) properties of the CDs were systematically examined using excitation wavelengths from 350 to 450 nm, covering the excitation range of potential fluorophores, subfluorophores, CD core/edge states, and surface states. As shown in Figure 1b, CDs exhibited a characteristic excitation-dependent emission profile, with the PL emission revealing two distinct spectral regions. Within the excitation range of 350–400 nm, an emission peak centered at 490 nm remained excitation-independent, suggesting the dominance of a single emissive transition. Upon excitation beyond 400 nm, a progressive red shift in the emission peak was observed, shifting to 520–550 nm, accompanied by a reduction in emission intensity. The excitation-dependent emission has been a widely reported phenomenon for CDs and holds important information about different transitions and emission centers.[50–53]

The photoluminescence (PL) data for CD solutions at varying concentrations (Figure 1c) reveal that CDs exhibit strong luminescence in dilute solutions; however, fluorescence intensity significantly diminishes in concentrated solutions. As concentration increases, the emission maxima undergo a pronounced red shift toward longer wavelengths, accompanied by a substantial reduction in intensity. This phenomenon, known as aggregation-caused quenching (ACQ), has been extensively documented for carbon dots (CDs) and arises from excessive direct π–π interactions or Förster resonance energy transfer (FRET).[9] In dilute solutions, the intermolecular distance (D) between CDs exceeds the Förster distance (R_n), preventing self-quenching. However, as D decreases below R_n, π-conjugated domains undergo stacking interactions, leading to an expanded conjugated π-electron system. This structural reorganization enhances energy dissipation, promoting fluorescence quenching. Additionally, the extension of π–π conjugation increases electron delocalization, reducing the band gap and inducing a red shift in the emission wavelength.[54]

To gain deeper insight into their photoluminescence (PL) properties, the pH-dependent behavior of CDs was examined under neutral, acidic, and alkaline conditions. As shown in Figure 1d, no significant changes were observed in either emission intensity or maxima, confirming that the luminescence of CDs remains unaffected from changes to pH. This stability highlights their effectiveness in tracking conformational transitions within polymeric matrices over a broad pH range, ensuring reliable visualization without interference.

Preparation of Polymer Brushes and Nanopatterned Templates

To evaluate the feasibility of brush-based stimuli responsive platforms incorporating CDs and to uncover the emergent collective properties of the resulting films, CDs were integrated with polymer brushes of three distinct compositions—poly(styrene-*alt*-maleic anhydride) (pSMA), poly(2-hydroxyethyl methacrylate) (pHEMA), and poly(N-isopropylacrylamide-*co*-2-hydroxyethyl methacrylate) (p(NIPAM-*co*-HEMA)). To integrate amine-functionalized carbon dots (CDs) within the brush architectures, tailored conjugation strategies were employed based on the distinct chemical functionalities of each polymer system (Scheme S1). In pSMA brushes, covalent immobilization was achieved via amine-anhydride reactions, forming stable amide linkages. For pHEMA and p(NIPAM-*co*-HEMA) brushes, dynamic

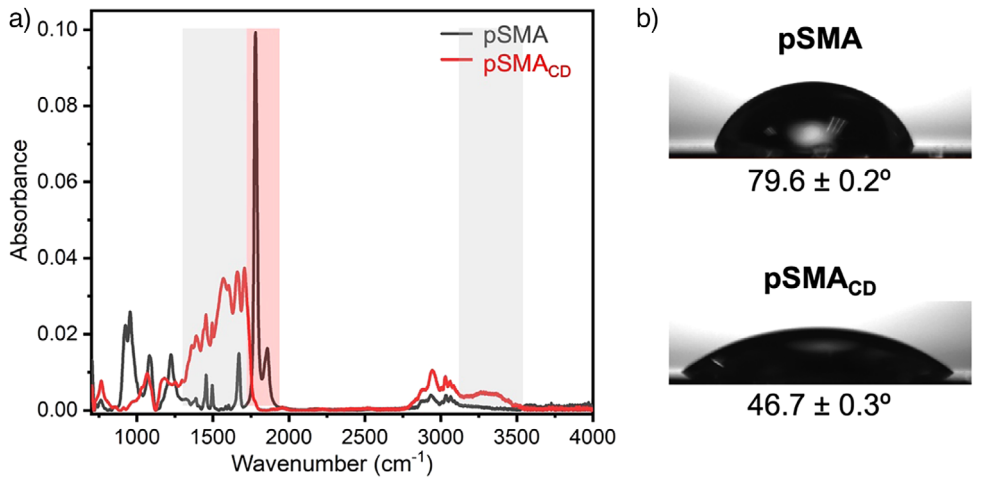

Figure 2. Characterization of pSMA brushes before and after CD immobilization. a) FT-IR spectra of pSMA and pSMA$_{CD}$. b) WCA of pSMA (top) and pSMA$_{CD}$ (bottom).

covalent interactions were facilitated through Schiff base chemistry, requiring a postpolymerization modification to introduce benzaldehyde moieties into the brushes. In aqueous environments, benzaldehyde-induced steric effects and hydrophobicity may confine binding reactions to the substrate surface without altering bulk chemistry. To address characterization challenges at low concentrations,[55] pHEMA brushes were used as model systems, providing a high density of binding sites for efficient detection.

pSMA brushes were synthesized via surface-initiated radical polymerization (SI-RP), grafted from both patterned and nonpatterned substrates that were prefunctionalized with an azo initiator, following a previously reported protocol.[42] Uniform pSMA brushes with a dry thickness (h_n) of 142 ± 3 nm were obtained after 1.5 h of polymerization. (Figure S2). Upon covalent immobilization of amine-functionalized CDs via amine-anhydride coupling, the brush thickness increased significantly, reaching 243 ± 2 nm, which directly correlates with the mass uptake.[56] As shown in Figure 2a, the Fourier transform infrared (FT-IR) spectrum of the unmodified pSMA brush exhibits strong absorption peaks at 1861, 1778, and 1226 cm^{-1}, corresponding to the asymmetrical and symmetrical stretching vibrations of the C═O and C─O─C groups of the cyclic anhydride, respectively.[57] These peaks completely disappear after CD immobilization, confirming the reaction of anhydride groups. Concurrently, a broad absorption band emerged at 3450 cm^{-1}, attributed to the stretching vibrations of ─OH and ─NH groups formed upon ring opening.[58] Additional characteristic peaks appear at ≈ 1710 cm^{-1} (C═O stretching in newly formed esters), 1668 cm^{-1} (O═C─N stretching in amide bonds), and 1580 cm^{-1} (─NH bending), further validating the successful conjugation of CDs within the polymer matrix. The water contact angle (WCA) of the pSMA brushes decreased markedly from 79.6 ± 0.2° to 46.7 ± 0.3°, indicating a substantial shift toward hydrophilicity (Figure 2b). This pronounced enhancement in wettability is a critical attribute for applications in solution-based systems, biosensing, and biomedical environments, where surface hydration and molecular interactions dictate performance. The XPS survey spectrum of the pSMA brush before modification exhibits C 1 s (285 eV) and O 1 s (533 eV) peaks. Following modification, the emergence of a pronounced N 1 s peak in the survey spectrum, along with an increased O content, confirms the immobilization of amine-functionalized CDs (Figure S3A,B). Premodification, the high-resolution XPS spectrum of C 1 s can be deconvoluted into three peaks at 284.8, 285.8, and 289.8 eV, corresponding to C═C, C─C, and O─C═O, respectively.[59] After modification, an additional component appeared, attributed to C─O/C─N bonds (Figure S3C,E).

To develop substrates enabling reprogrammable surfaces via dynamic covalent interactions, pHEMA and p(NIPAM-*co*-HEMA) brushes were synthesized using surface-initiated Cu(0)-mediated controlled radical polymerization (SI-CuCRP).[60] The resulting brush thicknesses were 155 ± 2 nm for pHEMA (Figure S4) and 292 ± 1 nm for p(NIPAM-*co*-HEMA) (Figure S5), with a surface roughness of less than 1 nm, confirming uniform polymerization and surface coverage. Subsequently, the samples underwent an esterification reaction with 4-carboxybenzaldehyde facilitating the incorporation of aldehyde functional groups as binding sites for Schiff base chemistry.[61]

Following esterification, pHEMA$_{BA}$ brushes displayed a 68% increase in thickness, reaching 260 ± 6 nm (Figure 3a**),** alongside a slight rise in surface roughness and WCA (Figure 3b) due to the introduction of aromatic rings (Figure S4). The FT-IR spectra of pHEMA and pHEMA$_{BA}$ are provided in Figure 3c. Postmodification, the substantial reduction of the broad ─OH stretching band at 3450 cm^{-1}, along with the intensified C═O stretching peak at 1728 cm^{-1} and the emergence of a distinct absorption band at 1716 cm^{-1},[62] confirms the effective conversion of hydroxyl groups into ester functionalities and the successful incorporation of aldehyde groups within the polymer structure. Moreover, the aldehyde C─H stretching peaks at 2740 and 2850 cm^{-1} provide compelling evidence of benzaldehyde functionalization, reinforcing the structural transformation of the polymer brush. The XPS survey spectrum of pHEMA$_{BA}$

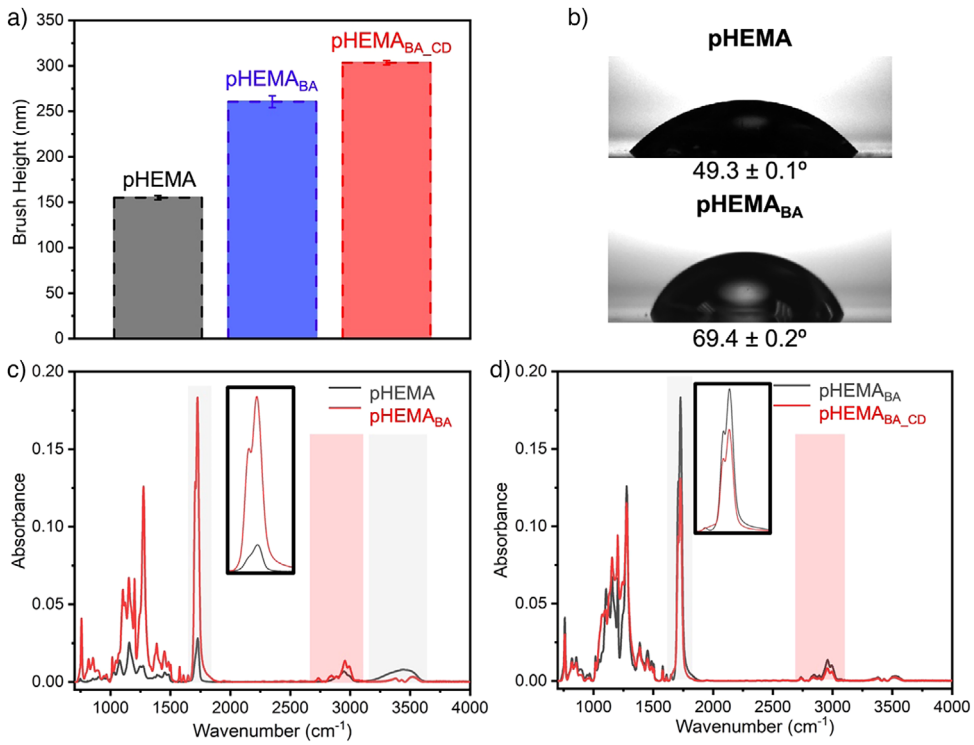

Figure 3. Characterization of pHEMA-based brushes before and after postpolymerization modification and CD immobilization. a) Brush height determined via AFM step-height measurements. b) WCA of pHEMA (top) and pHEMA$_{BA}$ (bottom). Overlay of FT-IR spectra for c) of pHEMA and pHEMA$_{BA}$ d) pHEMA$_{BA}$ and pHEMA$_{BA_CD}$.

reveals prominent C 1 s and O 1 s peaks, with a slightly increased C:O ratio compared to pHEMA (Figure S6A,B), further confirming surface modification.

The covalent attachment of CDs onto pHEMA$_{BA}$ brushes through dynamic imine bonds was initially verified by an increase in brush thickness (Figure 3a), which rose by 16%, reaching 303 ± 2 nm for pHEMA$_{BA_CD}$ (Figure S4). The limited height increase suggests that steric hindrance from benzaldehyde moieties restricted CD diffusion within the brush matrix. Spectral changes further confirmed the Schiff base reaction, as evidenced by the weakening of the aldehyde C═O absorption at 1716 cm^{-1}, along with reduced intensity of the aldehyde C─H stretching peaks at 2968 and 2898 cm^{-1}(Figure 3d). The formation of the imine bond was validated by the emergence of a distinct vibrational band at 1650 cm^{-1},[63] indicating the successful integration of CDs within the brush structure. Additionally, the XPS survey spectrum of pHEMA$_{BA_CD}$ reveals an N 1 s peak alongside C 1 s and O 1 s signals (Figure S6C), with core-level C 1 s and N1s analyses substantiating the structural transformations before and after CD immobilization (Figure S6D–G).

p(NIPAM-*co*-HEMA) brushes, with a HEMA:NIPAM ratio of 1 to 0.67 exhibited a 20% increase in height following esterification reaction, yielding p(NIPAM-*co*-HEMA)$_{BA}$ brushes with a final thickness of 350 ± 4 nm (Figure 4a). pNIPAM was selected to establish a thermoresponsive matrix, leveraging its characteristic behavior governed by a lower critical solution temperature (LCST). Therefore, preserving the thermoresponsive characteristics of pNIPAM segments after copolymerization with HEMA and subsequent benzaldehyde functionalization is essential for fabricating thermochromic films and patterns capable of generating optical responses. To systematically evaluate these properties, the WCA of p(NIPAM-*co*-HEMA) and p(NIPAM-*co*-HEMA)$_{BA}$ brushes was measured using a temperature-controlled stage (Figure 4b). For both samples, a noticeable shift in WCA was observed as the temperature increased from 5 to 25 °C, indicating the intricate interplay of hydrogen bonding, which drives conformational changes and dynamically modulates hydrophilicity and hydrophobicity.[64,65] Benzaldehyde functionalization led to an increase in the WCA; however, the thermoresponsive behavior was preserved. To further investigate this behavior, p(NIPAM-*co*-HEMA)$_{BA}$ brushes were analyzed between 5 and 25 °C at 5 °C intervals (Figure S7). FT-IR analysis confirmed the successful functionalization of p(NIPAM-*co*-HEMA) brushes with benzaldehyde moieties (Figure 4c). The carbonyl peak at 1730 cm^{-1} exhibited a significant contribution from newly formed C═O stretching vibrations, while the peak at 1712 cm^{-1} was attributed to the aldehyde C═O stretch. Additionally, the pronounced reduction in the broad peak around 3330 cm^{-1} suggested the conversion of ─OH groups into ester functionalities.

The immobilization of CDs resulted in a 9% increase in brush height. Despite the lower fraction of available binding sites in the copolymer structure compared to pHEMA$_{BA}$ brushes, the successful formation of imine bonds via Schiff base chemistry was confirmed through the analysis of characteristic spectral changes in the involved chemical groups

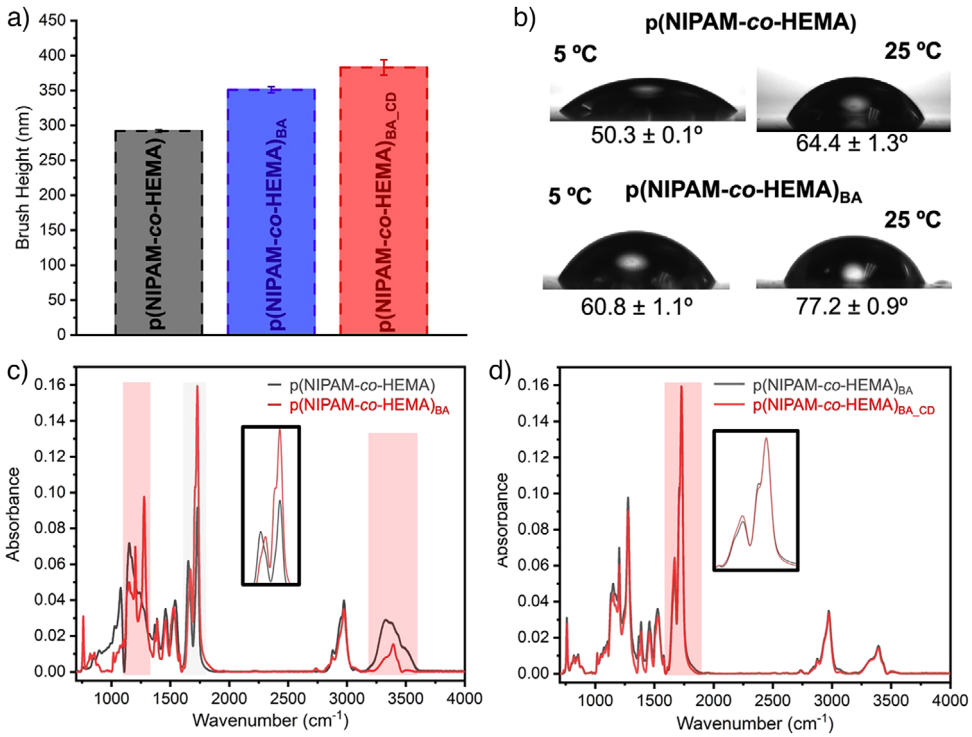

Figure 4. Characterization of p(NIPAM-*co*-HEMA)-based brushes before and after postpolymerization modification and CD immobilization. a) Brush height determined via AFM step-height measurements. b) WCA of p(NIPAM-*co*-HEMA) (top) and p(NIPAM-*co*-HEMA)$_{BA}$ (bottom) as a function temperature. Overlay of FT-IR spectra for c) p(NIPAM-*co*-HEMA) and p(NIPAM-*co*-HEMA)$_{BA}$ d) p(NIPAM-*co*-HEMA)$_{BA}$ and p(NIPAM-*co*-HEMA)$_{BA\_CD}$.

(Figure 4d). Specifically, the intensity of the aldehyde peak at 1712 cm^{-1} decreased, along with the peaks at 2749 and 2850 cm^{-1}, indicating aldehyde consumption. Concurrently, the intensity of the amide I peak at 1672 cm^{-1} increased,[66] likely due to the contributions of newly formed imine bonds and C=N stretching vibrations, as well as the functional groups of CDs that absorb in this region. XPS analysis further confirmed the successful immobilization of CDs onto p(NIPAM-*co*-HEMA)$_{BA}$ brushes. The survey spectra showed a significant increase in nitrogen content after CD attachment, verifying the incorporation of nitrogen-rich moieties, with core-level C 1 s and N 1 s spectra provided in the Supporting Information (Figure S8).

CD-Functionalized Responsive Nanoplatforms and Their Fluorescence Behavior

The synthesis of nanopatterned substrates followed the same methodology as unstructured films, yielding polymer brushes with precisely defined architectures and tunable dimensions ranging from 60 to 840 nm. Various patterns were designed to explore the potential for multiplex surfaces, integrating well-studied dot and line structures with established scaling relationships, alongside more intricate frame and nanoporous architectures.

Representative AFM images and corresponding height profiles of nanopatterned pSMA$_{CD}$ and p(NIPAM-*co*-HEMA)$_{BA\_CD}$ brushes, presented in Figures 5 **and** 6, respectively, provide detailed structural features of these patterned surfaces, highlighting variations in brush morphology and height distribution across different pattern designs. The comparatively lower thickness observed in nanopatterned brushes, relative to homogeneously grafted brush layers, is attributed to the reduced lateral confinement, which promotes chain relaxation and results in a less extended conformation. Brush thickness exhibited a pronounced dependence on pattern design, where variations in feature geometry directly influenced polymer chain conformation.[67,68] Although CD attachment led to a slight increase in brush height, the overall morphological integrity was preserved.

To confirm CD immobilization on the patterned brushes via Schiff base chemistry, a nanopatterned pHEMA$_{BA_CD}$ sample was mapped using AFM-IR at 1642 cm^{-1}, corresponding to the C=N stretching of imine bonds (Figure 6d–f). The 3D height profile overlaid with the IR map clearly demonstrates that IR absorption at 1642 cm^{-1} is localized exclusively within the patterned regions, confirming site-specific CD attachment through imine bond formation. Additionally, the AFM-IR signal intensity ratios of 1729 cm^{-1}/1642 cm^{-1} were evaluated at eight distinct locations and were consistently around 1:0.03, indicating a uniform distribution of functional groups and homogeneous grafting densities across the patterned surfaces (Figure S9)

Following the confirmation of successful CD immobilization on brush-modified substrates via spectral analysis and AFM measurements, the photophysical properties of the resulting films were systematically

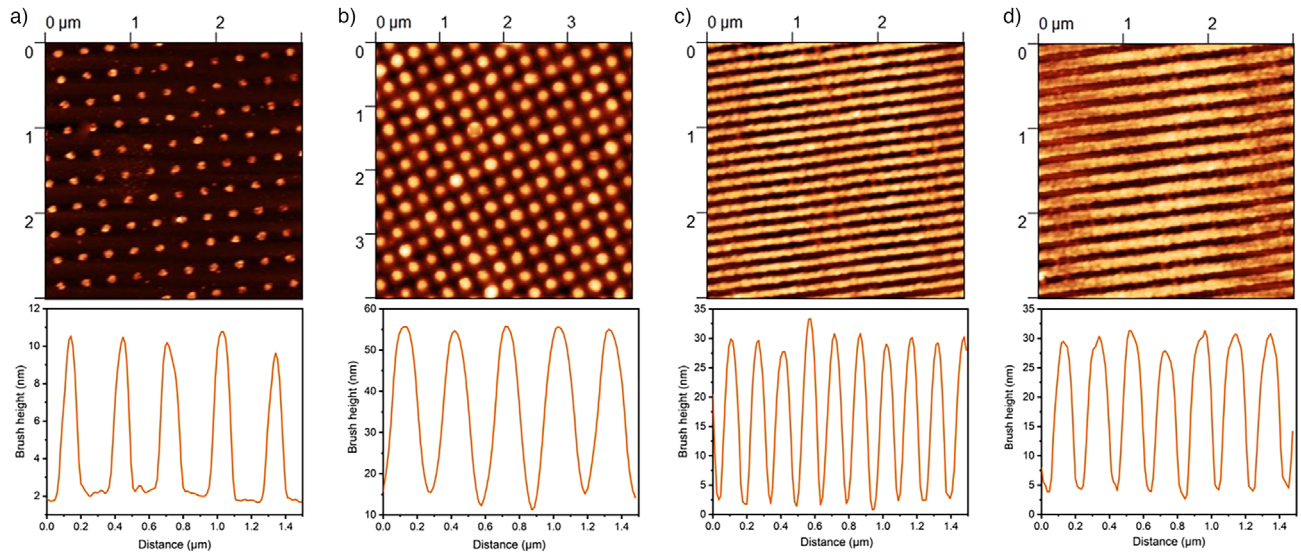

Figure 5. AFM height images of nanopatterned $pSMA_{CD}$ brushes and corresponding height profiles. a) Dot pattern with 70 nm diameter, 170 nm spacing and 9 nm thickness. b) Dot pattern with 220 nm diameter, 170 nm spacing, and 45 nm thickness. c) Line pattern with 80 nm line width, 60 nm spacing, and 25 nm thickness. d) Line Pattern with 110 nm line width, 60 nm spacing and 28 nm thickness.

examined using two-photon microscopy and IVIS Spectrum imaging system. As discussed earlier, polymer brushes were selected to serve as effective matrices for covalent CD immobilization, anticipated to fulfill multiple critical roles: incorporating stimuli-responsive components to regulate local CD concentration, ensuring homogeneous dispersion to prevent phase separation and aggregation, and introducing steric constraints that limit intramolecular rotation and vibration, thereby suppressing nonradiative transitions and enhancing fluorescence efficiency.[9] To validate the ability of polymer brushes to provide adequate spacing and steric hindrance in their most compact, dry/collapsed state—where FRET is more likely to occur due to smaller volume and shorter interparticle distance—a comparative fluorescence study was performed using the IVIS Spectrum imaging system under fluorescence mode. The sample with the highest CD content, $pSMA_{CD}$, was analyzed alongside a spin-coated film prepared from a concentrated CD solution. As illustrated in Figure S10, the spin-coated film exhibited fluorescence levels barely distinguishable from the background, attributed to excessive direct π–π interactions and fluorescence quenching via FRET resulting from the aggregation. In stark contrast, the $pSMA_{CD}$ films displayed intense and uniformly distributed fluorescence across the entire surface, demonstrating that polymer brush architectures effectively mitigate aggregation-induced quenching while preserving and enhancing the optical properties of immobilized CDs. After confirming that polymer brushes serve as optimal matrices for CD immobilization, their stimuli-responsive behavior was investigated to elucidate the interplay between brush conformation, steric effects, and optical response.

The pH-responsive behavior of $pSMA_{CD}$ brushes was systematically analyzed using liquid cell-AFM in buffer solutions with varying pH (Figure 7a). At pH 5, only a slight increase in brush thickness (≈6%) was observed, as the pH remained below the pK_a of the carboxyl-functionalized domains, resulting in limited hydration and minimal swelling. However, as the pH increased above the pK_a (5.5), the carboxylate groups deprotonated, triggering electrostatic repulsion and enhanced water uptake. Consequently, the brush thickness increased by 20% at pH 7 and 46% at pH 10 relative to the dry state, highlighting the increased hydrophilicity and charge-driven expansion of the brush network, which directly influences the spatial arrangement of the immobilized CDs and their optical properties. Examination of the samples under two-photon excitation (λ_{ex} = 800 nm) confirmed the two-photon excitation capability of CD-immobilized brushes, exhibiting a broad two-photon luminescence (TPL) spectrum spanning 413–700 nm. At pH 5, CDs confined within the pSMA matrix displayed a prominent emission peak centered at 582 nm, accompanied by a shoulder at ≈541 nm (Figure 7b), corresponding to yellow-green luminescence. As the brush network swelled, leading to the progressive dilution of immobilized CDs, the two-photon emission spectra decreased in fluorescence intensity and blue shifted from 582 to 541 nm, highlighting the direct influence of brush conformation on the optical properties of the embedded CDs (Figure 7c). The emergence of newly formed shoulders in the emission spectra can be attributed to the generation of additional energy levels upon CD immobilization within the polymer matrix. This confinement shortens the distance between functional groups, enhances electron cloud overlap, and strengthens coupling interactions, leading to the splitting of inherent energy levels and the formation of sublevels.[69] Additionally, the formation of covalent bonds between CDs and the matrix introduces new chemical interactions, further contributing to the development of distinct energy states.[9,22] Notably, when exposed to alternating pH 5 and pH 10 buffer solutions, the TPL intensity of the $pSMA_{CD}$ brushes exhibited remarkable reversibility over three consecutive cycles, as illustrated in Figure 7d. This cyclic response highlights the robustness and stability of the system, reinforcing the capability of the brush

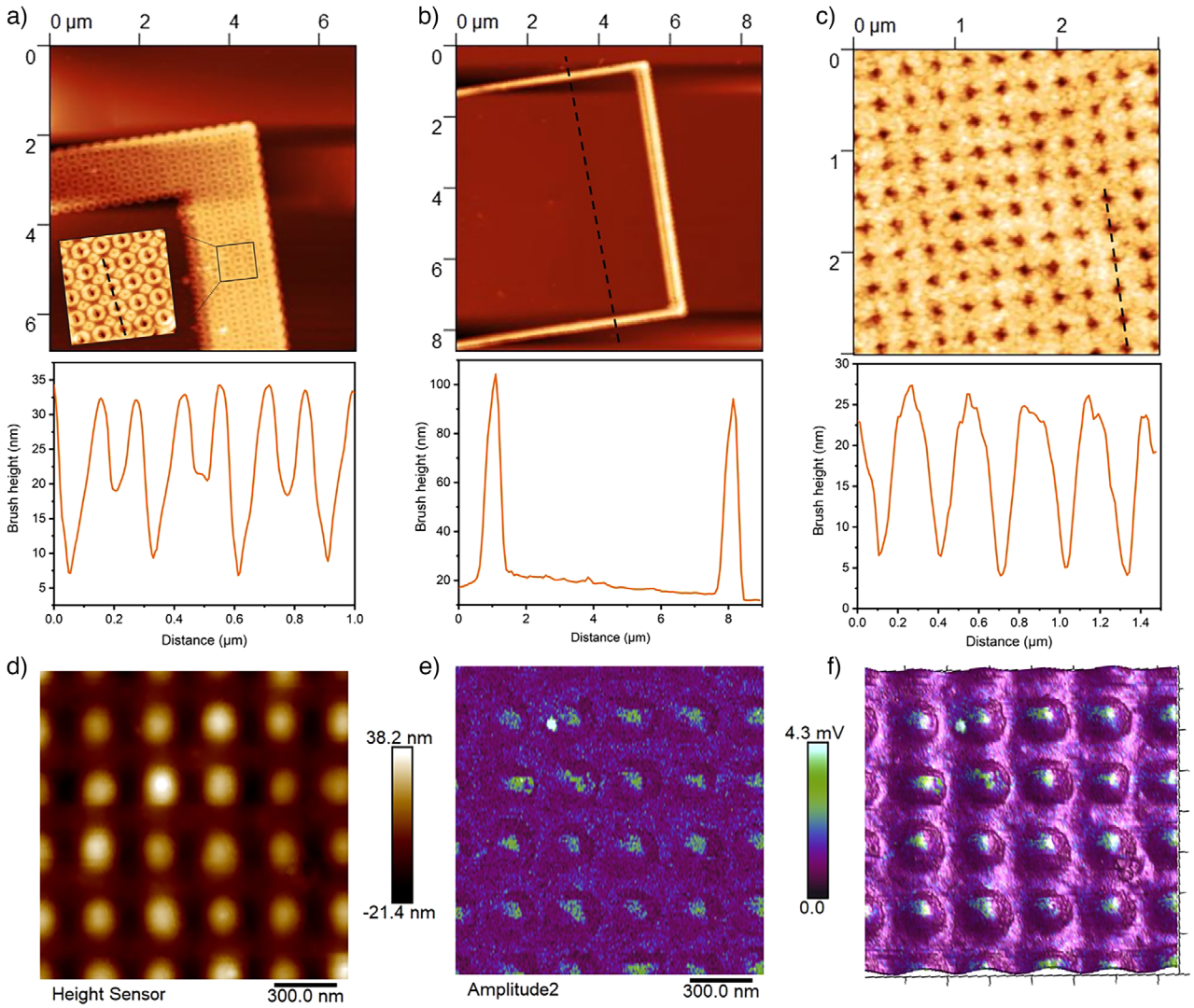

Figure 6. AFM height images of nanopatterned p(NIPAM-*co*-HEMA)$_{BA\_CD}$ brushes and corresponding height profiles. a) Frame pattern with a 2.1 μm frame width and 85 nm thickness, featuring 90 nm hollow details. b) Frame pattern with a 700 nm line width and an 80 nm brush thickness. c) Pattern with 80 nm diameter nanopores. d) AFM height image of the dot pattern with 100 nm diameter, 100 nm spacing. e) Corresponding AFM-IR chemical map at 1642 cm^{-1}, revealing the CD attachment to the patterned regions. f) 3D height profile overlaid with the IR map.

matrix to undergo reversible conformational transitions while preserving the optical integrity of the immobilized CDs.

The impact of steric effects was systematically explored using nanopatterned samples derived from pSMA brush templates with precisely tuned pattern designs. By modulating the initiator footprint size and center-to-center distance, we controlled the polymer chain density within defined regions, allowing for a detailed assessment of steric crowding, edge effects, and chain conformation. This strategic design provided crucial insights into how spatial constraints govern brush architecture, influencing not only the structural organization but also the optical behavior of immobilized CDs. In Figure 7c (bottom), a fluorescence image of the nanopatterned pSMA brushes featuring line patterns after CD immobilization is presented. Details of the nanopatterns, including line width and center-to-center spacing, are provided in the Supporting Information (Figure S11). The fluorescence intensity increased with line width, which directly correlates with the number of available binding sites, while it decreased with increasing center-to-center distance due to a lower local concentration of CDs and reduced interactions with subfluorophore moieties within the pSMA structure, such as heteroatom-containing double bonds.

The optical response of p(NIPAM-*co*-HEMA)$_{BA\_CD}$ brushes was evaluated under two-photon excitation in both the dry state and swollen state under increased humidity. As shown in Figures 8a, the brushes exhibited a reversible change in fluorescence intensity driven by water adsorption and desorption. Notably, while swelling influenced fluorescence intensity, it did not induce a shift in the emission maximum, which remained centered at approximately 541 nm in both states, suggesting that hydration modulates the local environment of the CDs without significantly altering their electronic structure (Figure 8b). Despite the low number of binding sites in the copolymer structure and the limited polymer volume in the patterned substrates, CD-immobilized

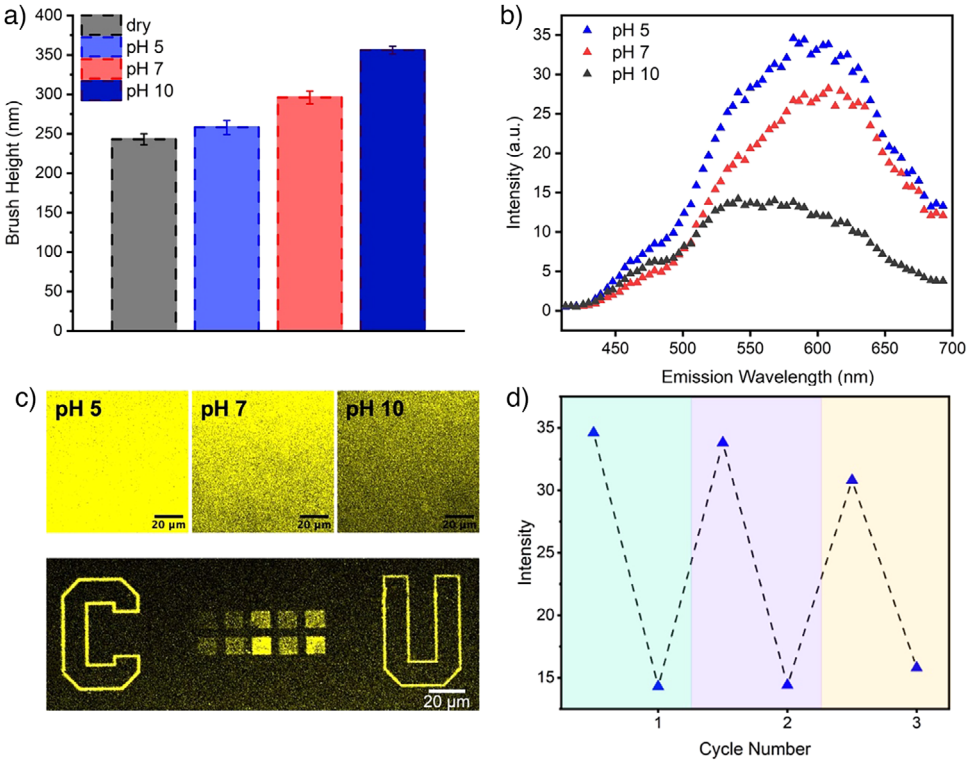

Figure 7. a) Dry and swollen heights of $pSMA_{CD}$ brushes determined via AFM step-height measurements. b) Fluorescence emission spectra of $pSMA_{CD}$ brushes in buffer solutions, collected using two-photon excitation microscopy (λex = 800 nm). c) Fluorescence images of $pSMA_{CD}$ brushes: top—samples in various solutions; bottom—nanopatterned brushes in pH 5. d) Alternating fluorescence intensity over three pH switching cycles.

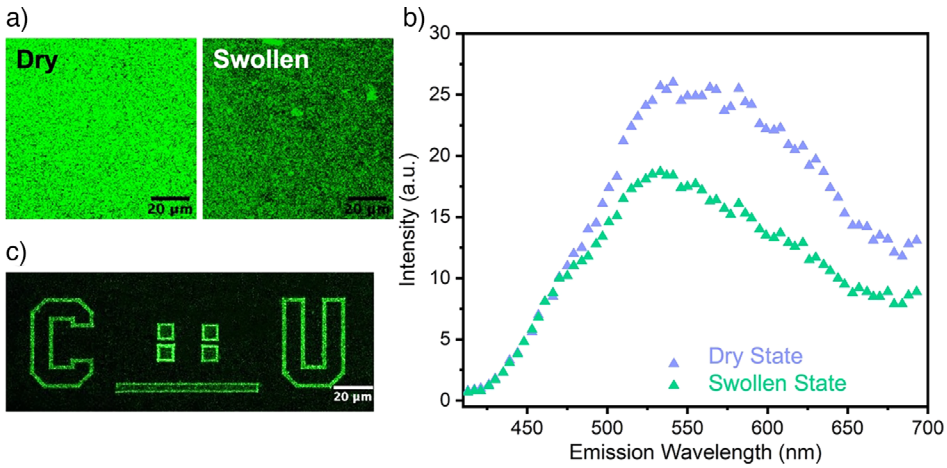

Figure 8. a) Fluorescence images of p(NIPAM-*co*-HEMA)$_{BA\_CD}$: top—samples in dry and swollen states. b) Fluorescence emission spectra of p(NIPAM-*co*-HEMA)$_{BA\_CD}$ in different states, collected using two-photon excitation microscopy (λex = 800 nm). c) Nanopatterned p(NIPAM-*co*-HEMA)$_{BA\_CD}$ brushes in pH 7.

p(NIPAM-*co*-HEMA)$_{BA\_CD}$ displayed bright fluorescence (Figure 8c). Schiff-base-mediated CD immobilization offers an effective and reversible approach for surface modification, facilitating dynamic "printing" and "erasing" of functional coatings.[70–72] Confocal microscopy analyses confirmed that the immobilized CDs could be removed via acid-catalyzed hydrolysis, demonstrating the reversibility of the Schiff-base linkage (Figure S12). This approach provides an adaptable method for creating rewritable surfaces with complex mixed gradients, enabling precise spatial control over chemical functionality.

Conclusion

In summary, by integrating polymer brushes with electron-beam lithography, we developed a versatile technique for immobilizing CDs to solid-state films, enabling the fabrication

of fluorescent films and nanopatterns with two-photon excitation. This method not only preserves the intrinsic properties of both the polymer matrices and CDs but also addresses the critical issue of aggregation-induced quenching, which has traditionally hindered the broader application of CDs. The ability to precisely control the local concentration and spatial arrangement of CDs is essential for fine-tuning their optical properties, a feature that is enabled through stimuli-induced conformational transitions and controlled steric crowding of polymer chains, dictated by the pattern design. Various chemistries have been explored to functionalize brush surfaces with optical reporters, demonstrating the feasibility of designing optically active, rewritable surfaces by leveraging the diverse chemical functionalities of polymer brushes. The direct covalent attachment of CDs via amine–anhydride reactions offers an efficient and scalable strategy, enabling higher loading capacities without the need for postpolymerization modification. Alternatively, dynamic covalent approaches— although limited by lower yields due to enhanced hydrophobicity and steric hindrance—offer the advantage of generating reprogrammable surfaces responsive to diverse external stimuli.

Notably, the two-photon luminescence observed in all samples further amplifies their potential for biosensing and bioimaging applications. This feature allows excitation via the simultaneous absorption of two lower-energy photons, significantly enhancing tissue penetration depth while reducing reliance on high-energy photons. As a result, it effectively mitigates photodamage, reduces photobleaching, and suppresses autofluorescence, making them highly advantageous for advanced optical bioapplications. These synergistic systems unlock transformative possibilities in nanoscale optics, responsive surfaces, advanced sensing platforms, and multifunctional coatings.

Acknowledgements

This study was primarily supported by the National Science Foundation through grant NSF CHE-2304838. The authors would also like to acknowledge the Center for Research on Programmable Plant Systems (CROPPS) for the financial support with major support from the National Science Foundation under Grant No. DBI 2019674. This work made use of the Cornell Center for Materials Research Shared Facilities and CESI Shared Facilities partly sponsored by the NSF MRI DMR-1338010 and Kavli Institute at Cornell and the Cornell NanoScale Facility, a member of the National Nanotechnology Coordinated Infrastructure (NNCI), which is supported by the National Science Foundation (Grant NNCI-2025233). The fluorescence characterizations made use of the Imaging facilities in Biotechnology Resource Center (BRC) at the Cornell Institute of Biotechnology (RRID:SCR_021741), with NYSTEM (C029155) and NIH (S10OD018516) funding for the shared Zeiss LSM880 confocal/multiphoton microscope and with NIH 1S10RR025502 funding for the shared Zeiss LSM 710 Confocal Microscope. The authors thank Dr. Jinhee Kim for assistance with AFM-IR measurements and Bruker for instrument access to the Dimension IconIR system. The authors thank Dr. Iosif Tantis for assisting with the XPS analyses of CDs.

Conflict of Interests

The authors declare no conflict of interest.

Data Availability Statement

The data that support the findings of this study are available from the corresponding author upon reasonable request.

Keywords: Carbon dots · Electron beam lithography · Polymer brushes · Two-photon luminescence

[1] R. Tutar, A. Motealleh, A. Khademhosseini, N. S. Kehr, *Adv. Funct. Mater.* **2019**, *29*, 1904344.
[2] A. Rao, S. Roy, V. Jain, P. P. Pillai, *ACS Appl. Mater. Interfaces* **2023**, *15*, 25248–25274.
[3] G. Devatha, A. Rao, S. Roy, P. P. Pillai, *ACS Energy Lett.* **2019**, *4*, 1710–1716.
[4] D. Venkatakrishnarao, C. Sahoo, R. Vattikunta, M. Annadhasan, S. R. G. Naraharisetty, R. Chandrasekar, *Adv. Opt. Mater.* **2017**, *5*, 1700695.
[5] R. A. Hughes, E. Menumerov, S. Neretina, *Nanotechnology* **2017**, *28*, 282002.
[6] R. Palankar, N. Medvedev, A. Rong, M. Delcea, *ACS Nano* **2013**, *7*, 4617–4628.
[7] S. W. Han, E. Jang, W.-G. Koh, *Sens. Actuators, B* **2015**, *209*, 242–251.
[8] C. Li, J. Yang, W. He, M. Xiong, X. Niu, X. Li, D.-G. Yu, *Adv. Mater. Interfaces* **2023**, *10*, 2202160.
[9] A. Xu, G. Wang, Y. Li, H. Dong, S. Yang, P. He, G. Ding, *Small* **2020**, *16*, 2004621.
[10] J. Ren, H. Opoku, S. Tang, L. Edman, J. Wang, *Adv. Sci.* **2024**, *11*, 2405472.
[11] J. Liu, R. Li, B. Yang, *ACS Cent. Sci.* **2020**, *6*, 2179–2195.
[12] F. Arcudi, L. Đorđević, *Small* **2023**, *19*, 2300906.
[13] Y. Liu, Z. Huang, X. Wang, Y. Hao, J. Yang, H. Wang, S. Qu, *Adv. Funct. Mater.*, *35*, 2420587.
[14] B. Wang, H. Cai, G. I. N. Waterhouse, X. Qu, B. Yang, S. Lu, *Small Science* **2022**, *2*, 2200012.
[15] L. Đorđević, F. Arcudi, M. Cacioppo, M. Prato, *Nat. Nanotechnol.* **2022**, *17*, 112–130.
[16] Y. Ru, G. I. N. Waterhouse, S. Lu, *Aggregate* **2022**, *3*, e296.
[17] C. Li, J. Li, Q. Teng, J. Li, F. Yuan, *Angew. Chem. Int. Ed.* **2025**, *64*, e202419983.
[18] J. He, Y. He, Y. Chen, B. Lei, J. Zhuang, Y. Xiao, Y. Liang, M. Zheng, H. Zhang, Y. Liu, *Small* **2017**, *13*, 1700075.
[19] X.-Y. Du, C.-F. Wang, G. Wu, S. Chen, *Angew. Chem. Int. Ed.* **2021**, *60*, 8585–8595.
[20] J.-Y. Wei, Q. Lou, J.-H. Zang, Z.-Y. Liu, Y.-L. Ye, C.-L. Shen, W.-B. Zhao, L. Dong, C.-X. Shan, *Adv. Opt. Mater.* **2020**, *8*, 1901938.
[21] H. Zhang, B. Wang, X. Yu, J. Li, J. Shang, J. Yu, *Angew. Chem. Int. Ed.* **2020**, *59*, 19390–19402.
[22] H. Wang, L. Ai, H. Song, Z. Song, X. Yong, S. Qu, S. Lu, *Adv. Funct. Mater.* **2023**, *33*, 2303756.
[23] L. Wang, X. Wang, H. Zhao, *Adv. Funct. Mater.*, 2423422.

[24] L. Pan, S. Sun, A. Zhang, K. Jiang, L. Zhang, C. Dong, Q. Huang, A. Wu, H. Lin, *Adv. Mater.* **2015**, *27*, 7782–7787.
[25] N. Naskar, W. Liu, H. Qi, A. Stumper, S. Fischer, T. Diemant, R. J. Behm, U. Kaiser, S. Rau, T. Weil, S. Chakrabortty, *ACS Appl. Mater. Interfaces* **2022**, *14*, 48327–48340.
[26] I. Ortiz-Gomez, M. Ortega-Muñoz, A. Marín-Sánchez, I. de Orbe-Payá, F. Hernandez-Mateo, L. F. Capitan-Vallvey, F. Santoyo-Gonzalez, A. Salinas-Castillo, *Microchim. Acta* **2020**, *187*, 421.
[27] Z. Wang, N. Jiang, M. Liu, R. Zhang, F. Huang, D. Chen, *Small* **2021**, *17*, 2104551.
[28] Y. Zhang, H. Song, L. Wang, J. Yu, B. Wang, Y. Hu, S.-Q. Zang, B. Yang, S. Lu, *Angew. Chem. Int. Ed.* **2021**, *60*, 25514–25521.
[29] S. Wu, H. Shi, W. Lu, S. Wei, H. Shang, H. Liu, M. Si, X. Le, G. Yin, P. Theato, T. Chen, *Angew. Chem. Int. Ed.* **2021**, *60*, 21890–21898.
[30] S. Qu, X. Wang, Q. Lu, X. Liu, L. Wang, *Angew. Chem. Int. Ed.* **2012**, *51*, 12215–12218.
[31] Q. Li, H. Zhao, D. Yang, S. Meng, H. Gu, C. Xiao, Y. Li, D. Cheng, S. Qu, H. Zeng, X. Zhu, J. Tan, J. Ding, *Nano Lett.* **2024**, *24*, 3028–3035.
[32] P. Long, Y. Feng, C. Cao, Y. Li, J. Han, S. Li, C. Peng, Z. Li, W. Feng, *Adv. Funct. Mater.* **2018**, *28*, 1800791.
[33] J. Wang, C.-F. Wang, S. Chen, *Angew. Chem. Int. Ed.* **2012**, *51*, 9297–9301.
[34] A. Segkos, I. Sakellis, N. Boukos, C. Drivas, S. Kennou, K. Kordatos, C. Tsamis, *Nanoscale* **2020**, *12*, 10254–10264.
[35] Y. Weng, Z. Li, L. Peng, W. Zhang, G. Chen, *Nanoscale* **2017**, *9*, 19263–19270.
[36] T. Chen, R. Ferris, J. Zhang, R. Ducker, S. Zauscher, *Prog. Polym. Sci.* **2010**, *35*, 94–112.
[37] S. Ma, X. Zhang, B. Yu, F. Zhou, *NPG Asia Mater* **2019**, *11*, 24.
[38] W.-L. Chen, R. Cordero, H. Tran, C. K. Ober, *Macromolecules* **2017**, *50*, 4089–4113.
[39] Y. Huang, H. Tran, C. K. Ober, *ACS Macro Lett.* **2021**, *10*, 755–759.
[40] J. Ge, L.-H. Rong, X. Cheng, Y. Tang, D. J. Pochan, E. B. Caldona, R. C. Advincula, *Macromolecules* **2025**, *58*, 3289–3297.
[41] U. Schmelmer, A. Paul, A. Küller, M. Steenackers, A. Ulman, M. Grunze, A. Gölzhäuser, R. Jordan, *Small* **2007**, *3*, 459–465.
[42] G. Aktas Eken, Y. Huang, O. Prucker, J. Rühe, C. Ober, *Small* **2024**, *20*, 2309040.
[43] E. C. Johnson, S. Varlas, O. Norvilaite, T. J. Neal, E. E. Brotherton, G. Sanderson, G. J. Leggett, S. P. Armes, *Chem. Mater.* **2023**, *35*, 6109–6122.
[44] Y. C. Kim, R. J. Composto, K. I. Winey, *ACS Nano* **2023**, *17*, 9224–9234.
[45] Y. Sekizawa, Y. Hasegawa, H. Mitomo, C. Toyokawa, Y. Yonamine, K. Ijiro, *Adv. Mater. Interfaces* **2024**, *11*, 2301066.
[46] A. Kiełbasa, K. Kowalczyk, K. Chajec-Gierczak, J. Bała, S. Zapotoczny, *Polym. Adv. Technol.* **2024**, *35*, e6397.
[47] Y. C. Kim, S. Hoang, K. I. Winey, R. J. Composto, *ACS Appl. Mater. Interfaces* **2024**, *16*, 61083–61095.
[48] A. Kouloumpis, E. Thomou, N. Chalmpes, K. Dimos, K. Spyrou, A. B. Bourlinos, I. Koutselas, D. Gournis, P. Rudolf, *J. Am. Chem. Soc.* **2012**, *134*, 747–750.
[49] M. Baikousi, N. Chalmpes, K. Spyrou, A. B. Bourlinos, A. Avgeropoulos, D. Gournis, M. A. Karakassides, *Mater. Lett.* **2019**, *254*, 58–61.
[50] J. Schneider, C. J. Reckmeier, Y. Xiong, M. von Seckendorff, A. S. Susha, P. Kasák, A. L. Rogach, *J. Phys. Chem. C* **2017**, *121*, 2014–2022.
[51] A. Sharma, T. Gadly, A. Gupta, A. Ballal, S. K. Ghosh, M. Kumbhakar, *J. Phys. Chem. Lett.* **2016**, *7*, 3695–3702.
[52] S. Zhu, Q. Meng, L. Wang, J. Zhang, Y. Song, H. Jin, K. Zhang, H. Sun, H. Wang, B. Yang, *Angew. Chem. Int. Ed.* **2013**, *52*, 3953–3957.
[53] P. Wang, M. Ge, X. Luo, Y. Zhai, N. Meckbach, V. Strehmel, S. Li, Z. Chen, B. Strehmel, *Angew. Chem. Int. Ed.* **2024**, *63*, e202402915.
[54] H. J. Yoo, B. E. Kwak, D. H. Kim, *J. Phys. Chem. C* **2019**, *123*, 27124–27131.
[55] A. S. Goldmann, N. R. B. Boase, L. Michalek, J. P. Blinco, A. Welle, C. Barner-Kowollik, *Adv. Mater.* **2019**, *31*, 1902665.
[56] H. Murata, O. Prucker, J. Rühe, *Macromolecules* **2007**, *40*, 5497–5503.
[57] M. Świtała-Żeliazkow, *Polym. Degrad. Stab.* **2001**, *74*, 579–584.
[58] Q. Zhang, Y. Gao, B. Luo, Y. Cui, S. Shu, W. Chen, L. Wang, *Polymers* **2023**, *15*, 952.
[59] A. Artemenko, A. Shchukarev, P. Štenclová, T. Wågberg, J. Segervald, X. Jia, A. Kromka, *IOP Conf. Ser.: Mater. Sci. Eng.* **2021**, *1050*, 012001.
[60] G. Aktas Eken, Y. Huang, Y. Guo, C. Ober, *ACS Appl. Polym. Mater* **2023**, *5*, 1613–1623.
[61] M. Wu, J. Chen, W. Huang, B. Yan, Q. Peng, J. Liu, L. Chen, H. Zeng, *Biomacromolecules* **2020**, *21*, 2409–2420.
[62] C. Ding, L. Zhao, F. Liu, J. Cheng, J. Gu, S. Dan, C. Liu, X. Qu, Z. Yang, *Biomacromolecules* **2010**, *11*, 1043–1051.
[63] A. Bhattacharya, N. K. Devaraj, *ACS Nano* **2019**, *13*, 7396–7401.
[64] Y. Li, J. Luo, G. Xie, D. Zhu, C. Zhao, X. Zhang, M. Liu, Y. Wu, Y. Guo, W. Yu, *ACS Appl. Polym. Mater* **2025**, *7*, 1–11.
[65] S. Tymetska, Y. Shymborska, Y. Stetsyshyn, A. Budkowski, A. Bernasik, K. Awsiuk, V. Donchak, J. Raczkowska, *ACS Biomater. Sci. Eng.* **2023**, *9*, 6256–6272.
[66] H. M. N. Ahmad, G. Dutta, J. Csoros, B. Si, R. Yang, J. M. Halpern, W. R. Seitz, E. Song, *ACS Appl. Polym. Mater* **2021**, *3*, 329–341.
[67] W.-K. Lee, M. Patra, P. Linse, S. Zauscher, *Small* **2007**, *3*, 63–66.
[68] Q. Yu, L. K. Ista, R. Gu, S. Zauscher, G. P. López, *Nanoscale* **2016**, *8*, 680–700.
[69] S. Zong, B. Wang, J. Zhang, X. Yu, Y. Zhou, Y. Chen, T. Zhang, J. Li, *Angew. Chem. Int. Ed.* **2025**, *64*, e202420156.
[70] L. Tauk, A. P. Schröder, G. Decher, N. Giuseppone, *Nat. Chem.* **2009**, *1*, 649–656.
[71] D. I. Rozkiewicz, B. J. Ravoo, D. N. Reinhoudt, *Langmuir* **2005**, *21*, 6337–6343.
[72] Y. Jia, J. Li, *Chem. Rev.* **2015**, *115*, 1597–1621.

Manuscript received: March 20, 2025
Revised manuscript received: April 17, 2025
Accepted manuscript online: April 21, 2025
Version of record online: ■■, ■■

Research Article

Polymer Brush

G. A. Eken*, N. Chalmpes, Y. Huang, E. P. Giannelis, C. Ober* —— **e202506448**

Nanoengineering Carbon Dot-Polymer Brush Interfaces for Adaptive Optical Materials

This study presents a platform for fabricating two-photon excitable carbon dot-based nanocomposite thin films using polymer brushes and electron-beam lithography. By mitigating aggregation-induced quenching and enabling dynamic optical modulation, these reprogrammable surfaces offer scalable integration into microchip technologies, biosensing platforms, and diagnostic systems.